Boundary-layer development on the afterbody of an engine nacelle

By EUGENE LAI AND L. C. SQUIRE

Cambridge University Engineering Department

Measurements have been made of the pressure distribution and turbulent-boundary-layer development on the afterbody of a model engine nacelle with a jet exhausting from the base and with the jet replaced by a parallel solid sting. It was found that the effect of replacing the jet by a solid body was to increase the pressure recovery over the afterbody and hence give a lower drag than with the jet. These changes in the pressure distribution affected the boundary-layer development and turbulence structure by different methods based on a momentum integral equation and the kinetic equation for the turbulence. Both methods approximately incorporate the effects of convergence and divergence of the flow caused by changes in transverse curvature of the surface. Neither method was completely satisfactory for the prediction of the overall boundary-layer development.

It was also found that, near the tail of the model, where the body radius is decreasing rapidly, the Reynolds shear stress was much lower than it would be in a two-dimensional boundary layer with the same pressure gradient. Calculations and analysis based on earlier work show that this reduction is directly related to the rates of strain associated with the convergence of the streamlines over the afterbody.

1. Introduction

In the estimation of the drag of a complete aircraft the calculation of the drag associated with the engine installation is particularly difficult and one critical area in this estimation is that of the nacelle afterbody drag. The flow in this region is marked by a very strong interaction between the viscous and the inviscid flows with the viscous flow being characterized by thick axisymmetric turbulent boundary layers, mixing shear layers and strong entrainment. Work on this topic has been in progress for the past few years with most of the effort being directed to a search for a simple method to simulate the jet, both in theoretical and experimental investigations. However, much less effort has been given to the study of the boundary-layer development on the afterbody and in particular there has been no work on any possible changes in this development associated with the methods used to simulate the jet.

The most commonly used method to simulate the jet is to treat it as a circular solid body. The effectiveness of this method has been studied by Reubush (1974) who conducted tests on a series of eight cylindrical plume simulators of different diameter. He concluded that: (*a*) the use of a jet-plume simulator resulted in a boat-tail pressure distribution close to the jet pressure distribution; (*b*) the boat-tail pressure distribution varied, but only slightly, with varying diameter of the simulator; and (*c*) the boat-tail drag with a jet simulator was less than that with an air jet at a nozzle pressure ratio (jet total pressure to free-stream static pressure) of 2. Abeyounis & Putnam (1980)

showed that as a result of jet entrainment the external flow field near the nozzle was strongly affected by the jet exhaust. Similar investigations on the validity of jet-exhaust-simulation techniques were made by Putnam & Abeyounis (1976) and by Wilmoth (1980). Their results generally confirmed the conclusions drawn by Reubush described above.

Until recently methods for the calculation of axisymmetric turbulent boundary layers were developed on the basis that the same methods were applicable to both two-dimensional and axisymmetric flows, that is the effects of convergence and divergence due to changes in lateral curvature of the surface (as governed by the parameter $(\delta/r)\,\mathrm{d}r/\mathrm{d}x$) and of lateral curvature on the boundary-layer structure (governed by δ/r) were ignored in the axisymmetric calculations. However, a number of recent investigations have shown that the turbulent-boundary-layer development in axisymmetric flows is directly affected by these effects (e.g. Chase 1972; Cebici 1970), and the effects of convergence and divergence owing to transverse curvature are included in more recent calculation methods (e.g. Bradshaw & Unsworth 1974; Green, Weeks & Brooman 1973). However, detailed boundary-layer measurements in axisymmetric flows are still needed to validate these recently developed boundary-layer calculation methods.

The development of a turbulent boundary layer near the tail of a body of revolution without a jet was investigated by Patel, Nakayama & Damian (1974). They observed a number of important characteristics of the flow in this region. (a) The boundary layer thickened very rapidly as a result of the decreasing body radius towards the trailing edge. (b) Significant variations in static pressure across the boundary layer indicated a strong interaction between the boundary layer and the potential flow. (c) The level of turbulence was abnormally low compared with that observed in a thin turbulent boundary layer proceeding towards separation. (d) The effect of transverse surface curvature was significant. Similar observations were made by Patel & Lee (1977) in thick axisymmetric turbulent boundary layers of a low-drag body of revolution.

Previous experimental investigations concerning the interaction between the flow surrounding an afterbody and a jet exhaust have mainly concentrated on one aspect of the problem; the jet-entrainment effects on the external flow field. Indeed, not a single reported test is known to the authors concerning jet-entrainment effects on turbulent-boundary-layer development on the afterbody. In an attempt to remedy this deficiency this paper presents the results of an experimental investigation of the boundary-layer development on a body of revolution with a jet issuing from the base. Detailed boundary-layer measurements (of both mean-flow and fluctuating quantities) were made with a jet velocity of 2.5 times the free-stream velocity and with the jet replaced by a solid circular sting approximately 4 jet diameters in length. These tests were made at a tunnel speed of 22 m/s, at which the Reynolds number based on body length was 1.47×10^6.

2. Details of the tests

2.1. *Model*

The main features of the model and the support system are shown in figure 1. The co-ordinates of the nacelle are given by

$$\frac{r}{L} = 0.5168\,\sqrt{X} - 0.6206X + 0.5031X^2 - 0.4956X^3 + 0.1437X^4, \quad 0 \leqslant X \leqslant 1.0.$$
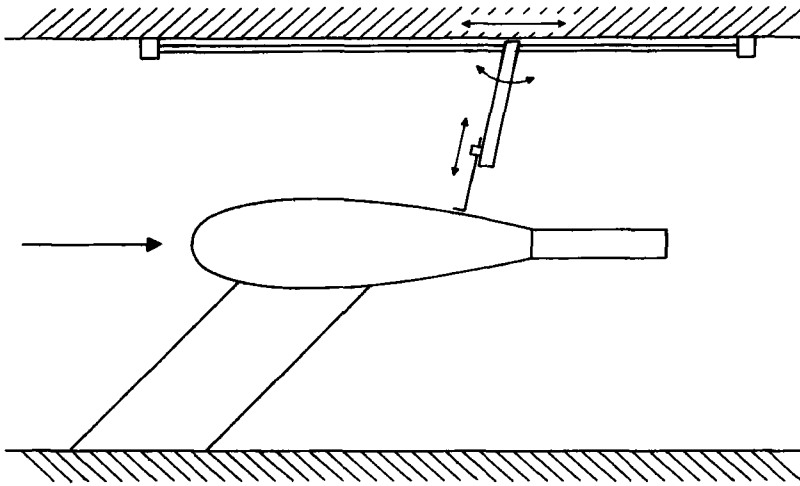
FIGURE 1. Sketch of model and traverse gear.
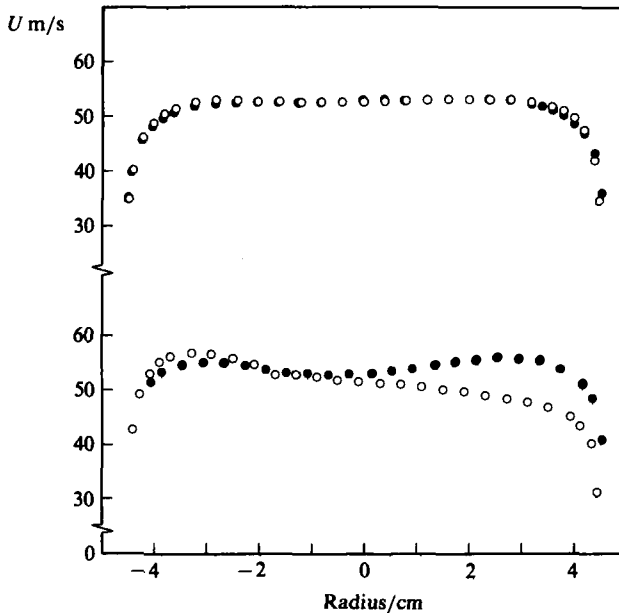
FIGURE 2. Jet profiles before (bottom) and after (top) fitting-
gauze: ○, vertical traverse; ●, horizontal traverse.

The model had a chord length L of 1 m and a maximum radius r/L of 0.131 at $X \equiv x/L = 0.38$. The shape had a parabolic nose, an almost parallel section over the centre region of the body, a 15° semi-angle afterbody and a square base. The model also had a 9 cm diameter circular internal passage running along the axis from mid-body to the base, for ducting compressed air. Thus the thickness of the annulus surrounding the jet at the base was 2.5 mm. The model was made of mahogany laminations and was supported by a 45° forward-swept metal strut.

The jet was created by exhausting compressed air into the tunnel through the strut

and the interior passage in the body. Initial tests showed that the velocity profiles in the jet just downstream of the base were not symmetric (figure 2). By a process of trial and error it was found that symmetric profiles could be obtained by inserting gauze into the passage. The gauze used was of 0.31 mm diameter wire with a mesh size of 3.175 mm. It was placed as far upstream as possible in the interior passage and covered only the top third of the passage. The resulting velocity profiles measured in the horizontal and vertical directions are shown in figure 2. During the tests the jet velocity was measured by a Pitot tube and a wall static hole placed inside the passage 150 mm upstream of the base. The air supply rate was controlled by a bypass valve and with this arrangement a nominal jet velocity of 55 m/s could be maintained to within 1.25 m/s.

The design of the strut system was based on a series of tests in a small tunnel. These tests showed that the swept-forward strut produced negligible disturbance to the pressure distribution and boundary-layer development over the upper half of the model, although it did produce some effect on the boundary-layer development on the lower half of the model.

2.2. Transition fixing

Initial tests using a stethoscope showed that natural transition occurred about half-way back along the nacelle, and it was therefore necessary to fix transition by a wire around the nose. This wire was of 0.56 mm diameter and was fixed to the surface at an axial distance of 47 mm (i.e. $x/L = 0.047$) from the hose. This produced transition just downstream of the wire as confirmed by noise levels and by a distinct change in the nature of the surface oil-flow patterns. Also, as will be seen below, the measured mean-velocity profiles at $x/L = 0.2$ were clearly turbulent with a well-defined logarithmic region.

2.3. Surface static-pressure measurements

Surface static pressures were measured along ten longitudinal generators which were numbered in a clockwise manner viewed from the front, with no measurements at 5 and 6 o'clock. Pressure tubes were let into the surface along each generator and the pressure distribution was measured by drilling and then filling holes along the tube. In all, 27 runs were needed to measure the pressure distribution along the entire body surface.

2.4. Traversing mechanism and probe systems

The traversing gear used is shown in figure 1. It consisted of a large and a small traverse gear pivoted together to provide three degrees of freedom. Streamwise motion was provided by manual movement of the large traverse gear bolted to the ceiling of the working section. Its total length of travel was 1.4 m and the range was sufficient to allow measurements to be made over 85 % of the body from $x/L = 0.15$ right up to the trailing edge. Traverse motion normal to the body surface was provided by the smaller gear, with a total travel of 60 mm. The inclination of this motion to the body surface was adjusted by manual rotation at the pivot and the actual motion was controlled by a flexible drive from outside the tunnel. The mechanism as a whole was thus capable of traversing a Pitot tube (or a hot-wire probe), in a direction normal to the body surface at required longitudinal locations on the top of the body (i.e. at 12 o'clock position). In order to reduce errors due to backlash the traverse was always moved away from the surface during tests and it

is estimated that the maximum error in the measured probe position over the full range of travel of 60 mm is ∓ 0.08 mm.

Total-pressure profiles were measured across the boundary layers using a flattened Pitot tube with a tip 1.59 mm wide and 0.13 mm thick (measured under a microscope). The initial, or zero, position of the probe with the tip just touching the surface was determined aerodynamically by gradually bringing the probe away from the wall and noting the position at which the probe pressure began to change appreciably. No pitch correction was applied since calibration showed that the correction was negligible, even at the rear of the model.

All Pitot pressures were measured relative to the static pressures on the body surface using a standard 250 mm-range Betz micromanometer capable of resolving pressure difference to within ± 0.01 mm water.

All electronic instrumentation used in the hot-wire anemometry was of standard design. The signals from the anemometer were first linearised, the output was then either filtered (for measuring turbulence intensities) with the low- and high-pass set at 0.5 Hz and 2.5 kHz respectively or fed (for measuring mean velocities) to a mini-computer programmed to yield velocities directly. This data-reduction system was devised by A. B. Duncan (private communication, 1981) using existing equipment and it has been shown to give excellent agreement with results obtained by a full-analog system.

Before the hot wire was calibrated for each run, the wind tunnel was run for about ten minutes at a velocity much higher than that used for making measurements in order to minimize the effect of hot-wire measurements of wind-tunnel air-temperature variations (Bradshaw 1971). This procedure contained the air-temperature variations to within ± 0.5 °C (without the jet) or ± 2.0 °C (with the jet) for a typical run which normally lasted between 60 and 90 min. These small variations were considered to be satisfactory and no attempt was made to control the temperature of the jet. At the end of each experiment, the probe was re-calibrated to check for possible drift in the electronics.

3. Surface-pressure distributions

Pressure distributions were measured along all ten generators for the following pairs of test conditions: (a) tests with the solid sting for tunnel speeds of 22 m/s and 28 m/s; (b) tests at the same tunnel speeds with solid stings of lengths 200 mm and 400 mm; and (c) tests at tunnel speeds of 22 m/s and 37 m/s with a jet velocity of 55 m/s.

In each pair of tests the measured pressure distributions were indistinguishable when plotted as pressure coefficients and so it could be concluded that within the range covered the results were independent of tunnel speed, sting length and jet/tunnel velocity ratio. It was thus decided to limit all further tests to a tunnel speed of 22 m/s (i.e. a Reynolds number based on length of 1.47×10^6), with either a jet velocity of 55 m/s (i.e. a jet/tunnel velocity ratio of 2.5) or with the jet replaced by a solid sting of length 400 mm. All pressure distributions were corrected for tunnel interference using conventional methods.

Measured pressure distributions along three generators at 9, 12 and 3 o'clock are presented in figure 3(a), where it can be seen that the flow over the upper half of the model is closely axisymmetric. Over the lower half of the model the effect of the strut is confined to the immediate vicinity of the strut/nacelle junction (figures 3b and c, with only a very small effect at the base of the model. Thus it would appear reasonable to assume that the flow at and near the 12 o'clock generator is unaffected by the
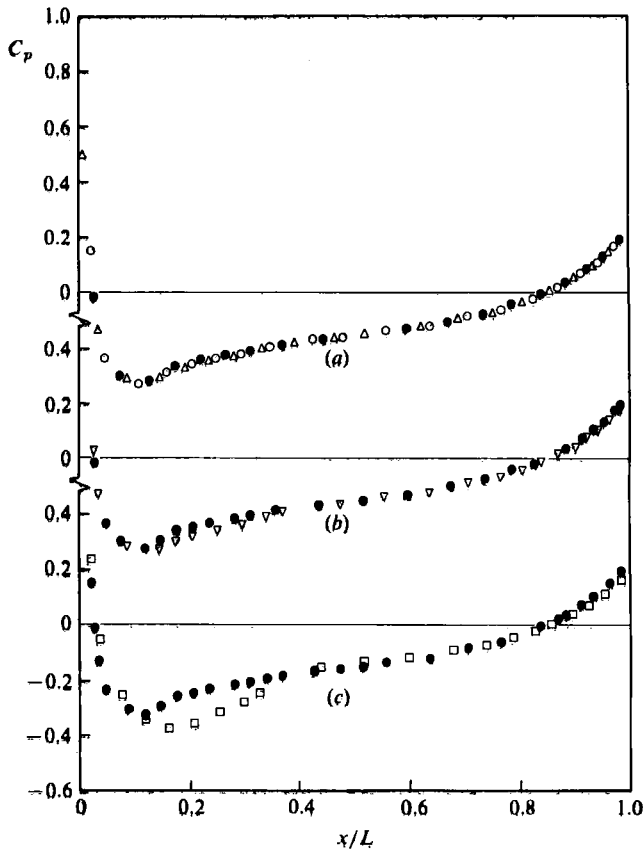
FIGURE 3. Comparison of longitudinal pressure distributions measured with the sting along various generators, (a) ◯, 3 o'clock; △, 9 o'clock; ●, 12 o'clock: (b) ▽, 8 o'clock; ●, 12 o'clock: (c) □, 7 o'clock; ●, 12 o'clock.

presence of the strut and can be taken as representative of axisymmetric flow over the nacelle.

Figure 4(a) shows the measured pressure distributions along this generator, i.e. along the top of the nacelle with the sting and with the jet. Over the first 85% of the length the pressure distributions are completely independent of the jet flow but near the base the pressure recovery with the sting is significantly greater so that, as in the test result of Reubush (1974), the drag of the nacelle with the jet is greater than with the jet represented by the sting. Also, as will be seen later, the skin friction on the afterbody is greater with the jet. The total increase in drag coefficient from both these sources was found to be 0.0084 (based on nacelle frontal area) of which less than 4% was owing to the change in skin friction. The actual mechanism for these changes will be considered below after the results of the boundary-layer measurements have been presented.

Figure 4(b) compares the measured pressures on the nacelle plus the sting with the results of various prediction methods. Thus the solid line represents the results calculated by a surface-singularity method developed by the first author (Lai 1983) using a distribution of ring sources along the nacelle and sting surface following the higher-order source techniques outlined by Hess & Martin (1974). The results shown in figure 4(b) were obtained by representing the body surface by 40 ring sources and
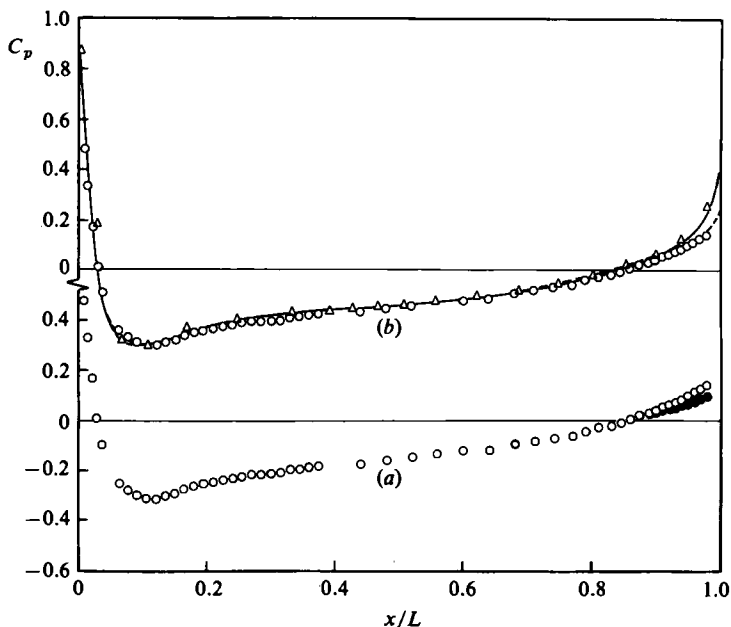
FIGURE 4. Comparison of measured pressure distributions along 12 o'clock generator with theoretical results: (*a*) measurements with jet, ●; and with sting, ○; (*b*) present calculations with (----) and without (——) viscous correction; △, British Aerospace calculations.

numerical checks showed that with this number of sources or more the results were independent of panel size and number. The figure also includes results calculated by British Aerospace using a fully three-dimensional-panel method for the flow over the model with its support strut. The close agreement between the two calculations again confirms that the flow over the top of the model is independent of the presence of the strut.

Over the first 85% of the length of the body the measured pressures are in close agreement with the calculated inviscid pressures, but over the rear the measured recovery is much less than that calculated, owing to the displacement effect of the boundary layer. This effect was calculated iteratively using a boundary-layer method developed by Bradshaw & Unsworth (1974). For the present case this method converged after five iterations and the results are in very good agreement with the measured pressures.

4. Boundary-layer measurements

4.1. *Mean-flow profiles*

Mean-velocity distributions across the boundary layer were measured at selected axial stations (table I) along the 12 o'clock generator with the sting and with the jet. A flattened Pitot tube was used at all eleven stations while a X-wire probe was used only at the last six stations (6–11) since its use was limited by its size in relation to the boundary-layer thickness.

Velocity distributions by means of the flattened Pitot tube at all eleven stations (with the sting) and at the last six stations (with the jet) are shown in figure 5. The shape of the velocity profile at station 1 ($x/L = 0.196$) is similar to that observed in

Station	1	2	3	4	5	6	7	8	9	10	11
x/L	0.196	0.441	0.661	0.741	0.809	0.848	0.888	0.917	0.946	0.965	0.985

TABLE 1. Axial positions of boundary-layer traverses
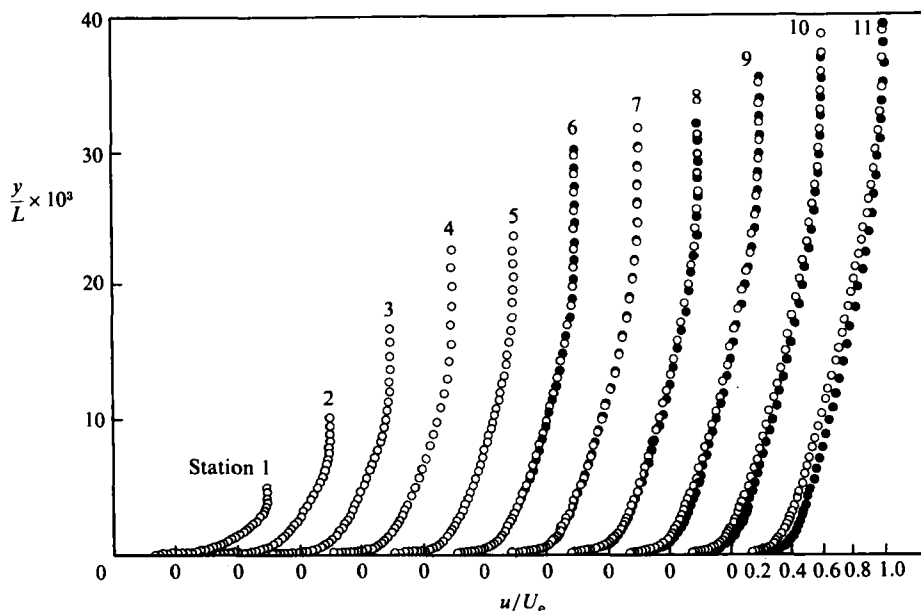
FIGURE 5. Mean-velocity profiles as measured by Pitot tube. $\bigcirc$, with sting; $\bullet$, with jet.

flows with mildly adverse pressure gradients (see e.g. Bradshaw 1966). The velocity profiles are observed to change slowly between stations 1 and 4 where the body surface is nearly flat. This is mainly attributed to the near-zero pressure gradient which prevails in that region ($0.2 \leqslant x/L \leqslant 0.75$). Further downstream the boundary-layer thickness is seen to increase rapidly under the joint influence of the decrease in body radius and the increasing adverse pressure gradient.

The velocity profiles measured with the sting and with the jet showed no discernible difference at station 6 ($x/L = 0.848$) but thereafter the boundary-layer profiles with the sting became increasingly less full than the profiles with the jet, a trend which would be expected from the greater adverse pressure gradient on the afterbody with the sting. In fact it was found that the *difference* between the two measured profiles at station 11 was predicted very closely by the boundary-layer-calculation method of Bradshaw & Unsworth (1974) given the measured pressure distributions (figure 6) although the overall prediction of the shape of the profile is less good. The fact that the changes are predicted with good accuracy suggests that the changes noted in figure 5 are a direct consequence of the change in pressure distribution on the afterbody and are not caused directly by any change in entrainment or turbulence level owing to the presence or otherwise of the jet.

The longitudinal components of the mean-flow velocity of the jet measured with the X-wire probe are compared with those obtained from the Pitot-tube measurements at the last six stations in figure 7; as will be seen the agreement between the two
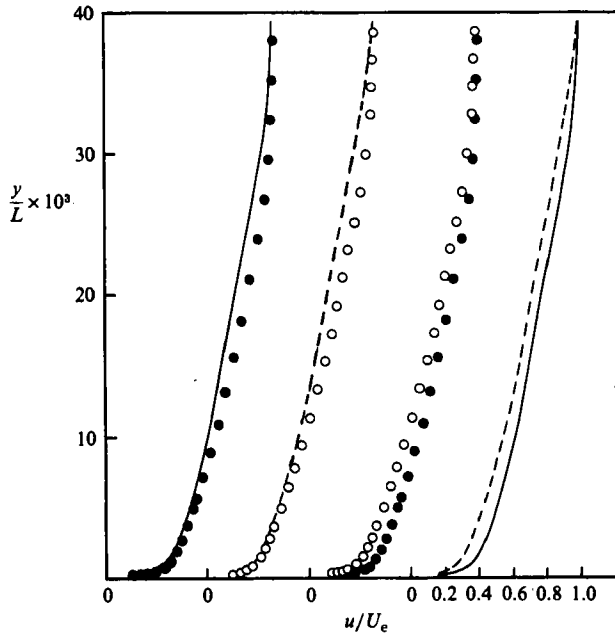
FIGURE 6. Comparison of measured profiles at station 11 with profiles calculated by the method of Bradshaw & Unsworth: ●, measured with jet; ○, measured with sting; ———, calculated with jet; ————, calculated with sting.
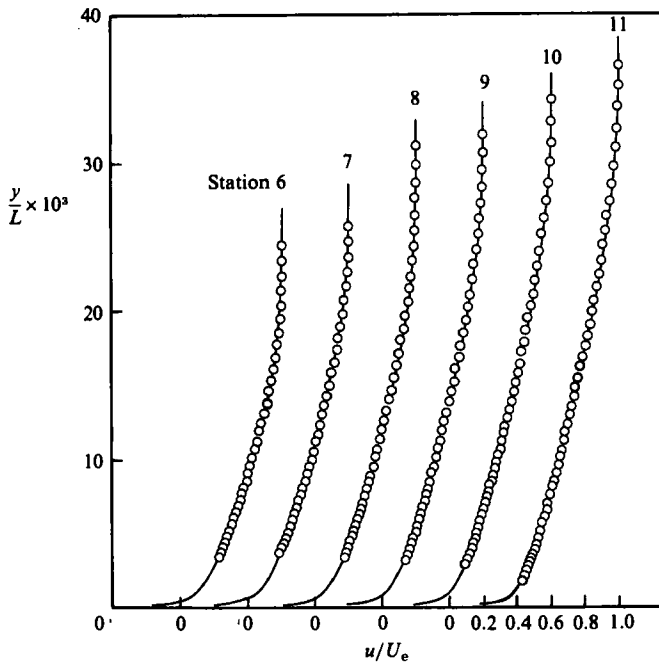
FIGURE 7. Comparison of mean-velocity profiles with the jet as measured by the Pitot tube, ○; and by the hot wire, ———.
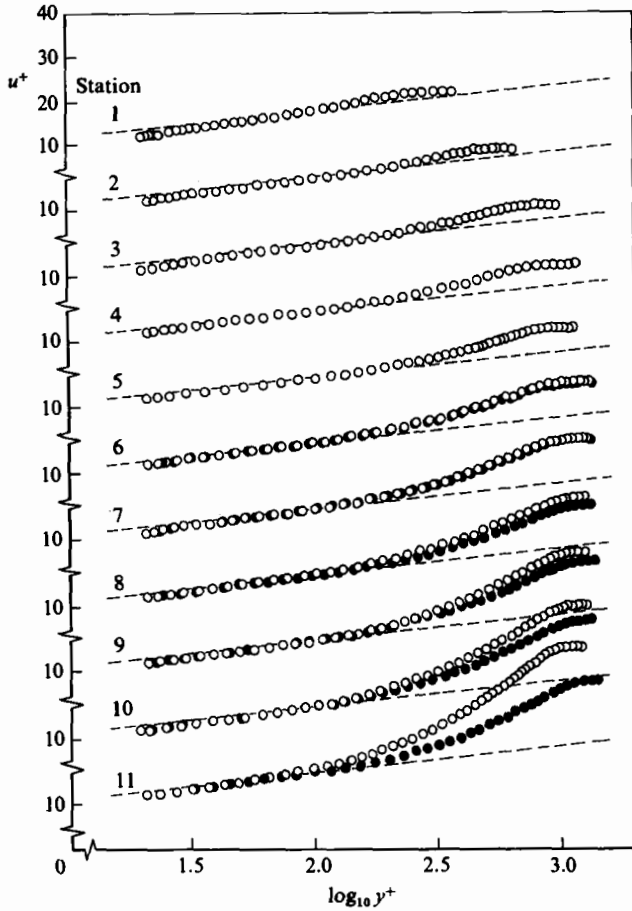
FIGURE 8. Law-of-the-wall plot: $\bigcirc$, with the sting;
$\bullet$, with the jet; $---$, $u^+ = 5.76 \log_{10} y^+ + 5.5$.

methods of measurement is excellent and similar agreement was found for measurements with the sting. This good agreement shows that the variation of static pressure across the layer has a negligible effect on the measured velocity profiles as deduced from the Pitot-tube readings. (It should be noted that measurements obtained near the wall at the last station should be treated with caution since the lower part of the probe stem was either in the path of the jet or was submerged in a slot in the sting. The region so affected is in the range $0 < y/L < 0.005$.)

Velocity distributions measured with the sting are plotted in wall co-ordinates $u^+ = u/u_\tau$, $y^+ = yu_\tau/\nu$ in figure 8 using values of the skin friction given by the Clauser plot (figure 9). Also shown are velocity distributions measured with the jet at the rear six stations and the two-dimensional logarithmic law $u^+ = 5.76 \log_{10} y^+ + 5.5$ All the profiles have a clearly defined semi-logarithmic region near the wall, although this region is very small at the first station, where the wake component is also small. At this station the boundary layer had just passed through a region where the pressure gradient is favourable and the flow is divergent; thus departures from the logarithmic law would be expected. Also the value of R_θ is about 500, so a small wake component would also be expected. Towards the rear of the model the wake component increases as the pressure gradient becomes more adverse and R_θ increases.
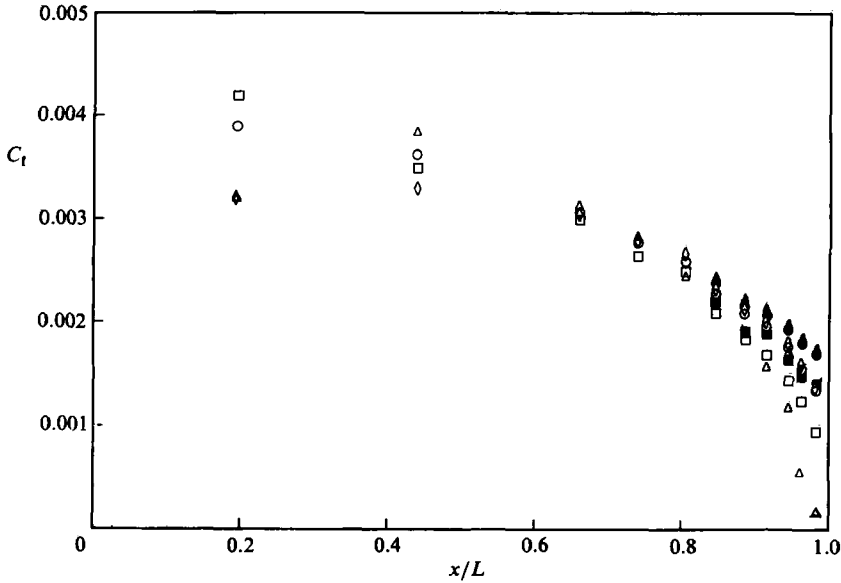
FIGURE 9. Variation of skin-friction coefficients along the body: □, Clauser plot; ○, Thompson; ◇, Ludwieg & Tillmann; △, Bradshaw & Unsworth. Open symbols with sting, solid symbols with jet.

4.2. *Wall shear stress*

Since no direct skin-friction measurements were made the wall shear stress τ_w was deduced by applying the method of Clauser (1954) to the pitot mean-velocity profile at each station. For convenience, the velocity distributions for the wall region proposed by Spalding (1961) were used in preference to the normal log law,

$$y^+ = u^+ + e^{-kB}\left(e^{ku^+} - ku^+ - \frac{(ku^+)^2}{2} - \frac{(ku^+)^3}{6}\right),$$

where $k = 0.4$ and $B = 5.5$, since this equation approximates the velocity distributions for the whole of the inner region. Figure 9 shows the comparison of the values of the skin-friction coefficient $C_f = \tau_w/\frac{1}{2}\rho U_e^2$ obtained from (a) the Clauser plots, (b) the charts of Thompson (1965), and (c) the skin-friction formula of Ludwieg & Tillmann (1949)

$$C_f = 0.246\left(\frac{U_e\theta}{\nu}\right)^{-0.268} 10^{-0.678H}.$$

Results from the Bradshaw & Unsworth program are also shown. The significant disagreement between C_f values seen at station 1 is probably attributable to (a) the relatively large upstream flow influences owing to the body geometry, so that the flow at station 1 does not resemble plane two-dimensional flow; and (b) the low Reynolds number in this region so that results obtained from both Ludwieg & Tillmann's formula and Thompson's charts may be unreliable. Also, in axisymmetric flows the low-Reynolds-number allowance in the Bradshaw & Unsworth method may be inappropriate. Between stations 1 and 3 the Reynolds number increases ($R_\theta = 2000$ at station 3) and the flow gradually relaxes back to normal plane two-dimensional flow, so that excellent agreement is observed at station 3. However, appreciable disagreement is seen to re-emerge downstream of $x/L = 0.8$ where the boundary layer

E. Lai and L. C. Squire
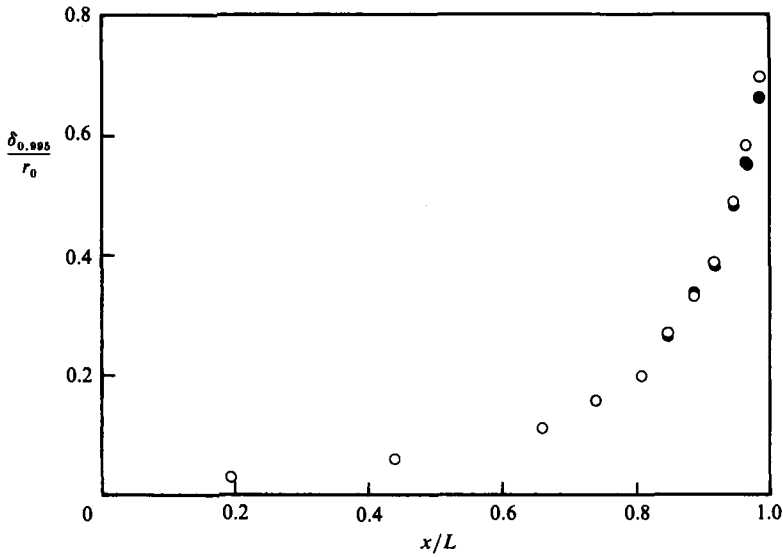
FIGURE 10. Variation of ratio of boundary-layer thickness to body
radius along body: ○, with sting; ●, with jet.
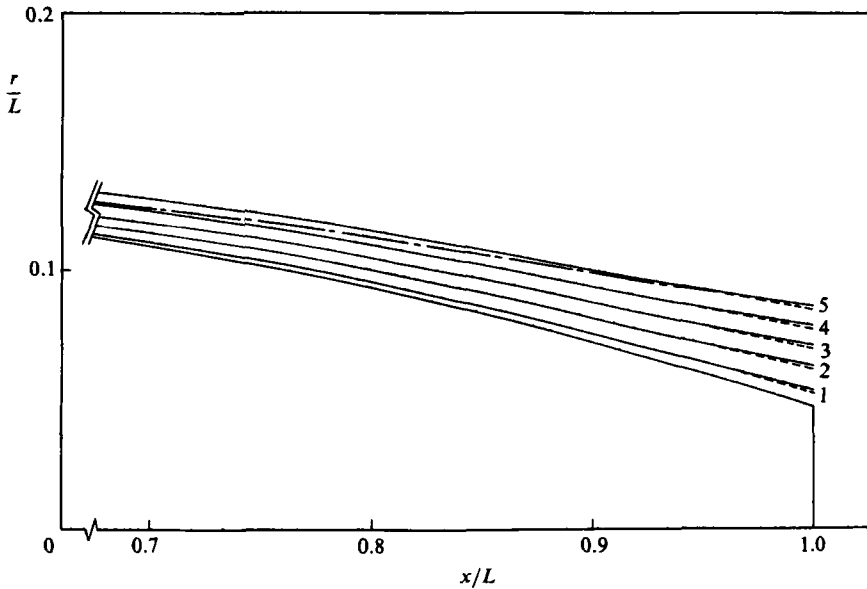
FIGURE 11. Comparison of mean-flow streamlines computed from Pitot-tube measurements:
———, with sting; ----, with jet; —————, $\delta_{0.995}$.

$$
\begin{array}{cccccc}
 & 1 & 2 & 3 & 4 & 5 \\
\psi/(U_e L^2) = & 0.0001 & 0.0004 & 0.0008 & 0.0013 & 0.0019
\end{array}
$$

thickens rapidly. The discrepancies between C_f values seen in the tail region may be attributed to the inadequacy of the well-known two-parameter representation for describing the mean-velocity profiles in thick axisymmetric boundary layers. As will be seen, the value of C_f as calculated by the Bradshaw & Unsworth program is in reasonable agreement with the other values over the first 90 % of the body. Right at the rear it predicts very low values of C_f with boundary layers just on the point

of separation. However, the skin-friction coefficient in the tail region increases significantly in the presence of the jet whichever way the skin-friction coefficient is obtained. It should be noted that the values of C_f derived from the Ludwieg–Tillmann formula are only slightly dependent on the definitions (see Appendix) used to calculate θ and H.

4.3. *Integral parameters*

The thickness δ of the boundary layer is defined as the normal distance from the wall where the local velocity is 0.995 times the free-stream velocity and was determined from the Pitot mean-flow measurements. Its magnitude in relation to the local radius of the body δ/r_0 is shown in figure 10. Detailed measurements made by Patel, Nakayama & Damian (1974) in thick axisymmetric boundary layers showed that for $\delta/r_0 > 0.4$ static pressure varied appreciably across the boundary layer, particularly where the local longitudinal surface curvature was large. Figure 10 shows that the value of δ/r_0 over the first 85 % of the body length is less than 0.4, but it increases rapidly over the last 15 %. Thus near the base of the model there may be significant variations in static pressure across the layer.

The mean-flow streamlines were obtained from the Pitot measurements by computing the distribution of the stream function ψ at each station,

where
$$\psi(y) = \int_0^y ru \, dy \quad \text{and} \quad r = r_0 + y \cos\phi.$$

The distributions of the stream function ψ in the neighbourhood of the afterbody with and without the jet are shown in figure 11. It can be seen that the streamlines are nearly parallel to the body surface but are increasingly divergent as the boundary layer thickens. The entrainment of inviscid fluid into the boundary layer is observed to be small in the thick boundary layer near the tail of the body. This is indicated by the position of the streamlines relative to the edge of the boundary layer. It can also be seen that the streamlines become more divergent in the tail region when the jet is replaced by a sting, so much so that the streamline curvature changes from convex to concave near the trailing edge for the sting.

Figures 12–14 show the variations of the various integral parameters along the body. In each figure the top set of results compares the planar and axisymmetric (see Appendix) values of the appropriate integral parameter for the flow with the sting and the middle set compares corresponding results for the flow with the jet. The lower set compares flows with the sting and the jet using the axisymmetric definition of the integral parameter. At the base of the model where the boundary layer is thick the thicknesses based on the axisymmetric definition are significantly greater than those based on the planar definition with the difference being greater for the displacement thickness. Thus shape factors based on the axisymmetric definitions are slightly greater than those based on planar definitions.

In the comparison of the results with the sting and the jet the thicknesses with the sting are greater than those with the jet, as is the shape factor. This trend corresponds to the larger adverse pressure gradient in the flow without the jet and in fact as noted above it was found that the differences between the results with the sting and with the jet were closely predicted by two boundary-layer calculation methods. This, again, confirms that the changes in boundary-layer development associated with the presence of the jet are directly related to the resultant changes in external velocity, and hence in the pressure distribution along the body.

It should also be noted that irrespective of definition, or presence of the jet, the
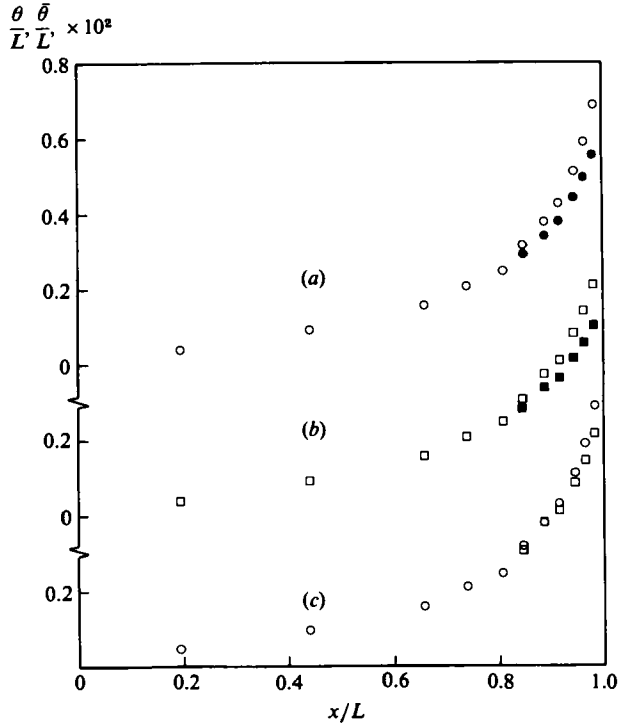
FIGURE 12. Variation of momentum thickness along the body, (a) with the sting, $\bigcirc$, (b) with the jet, $\square$, (c) with sting and jet. Open symbols for axisymmetric definitions; solid symbols for planar definitions.
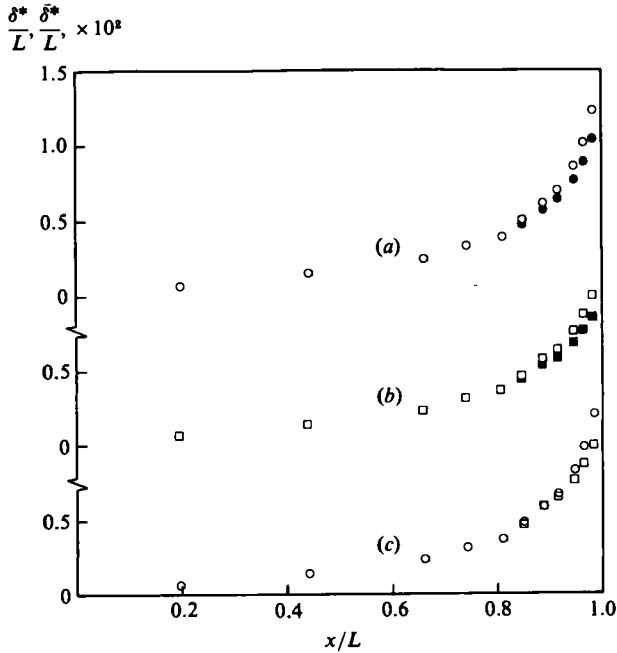
FIGURE 13. Variation of displacement thickness along the body. Key as figure 12.
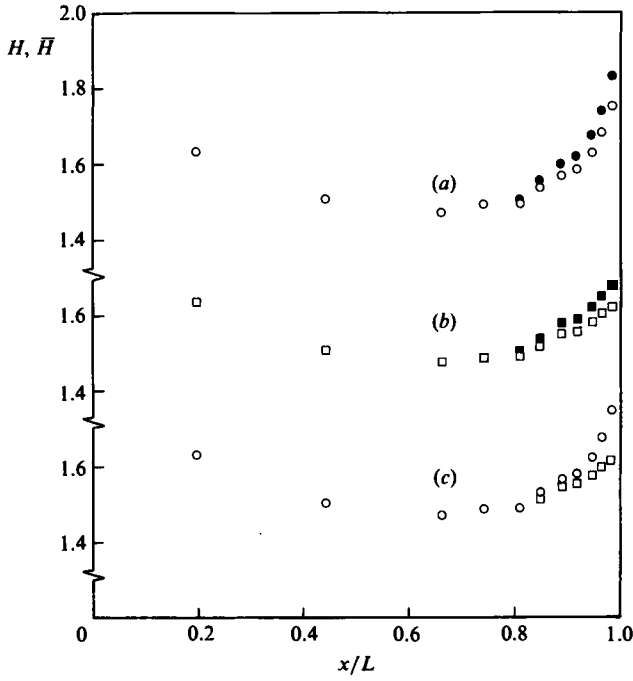
FIGURE 14. Variation of shape factor H along the body. Key as figure 12.
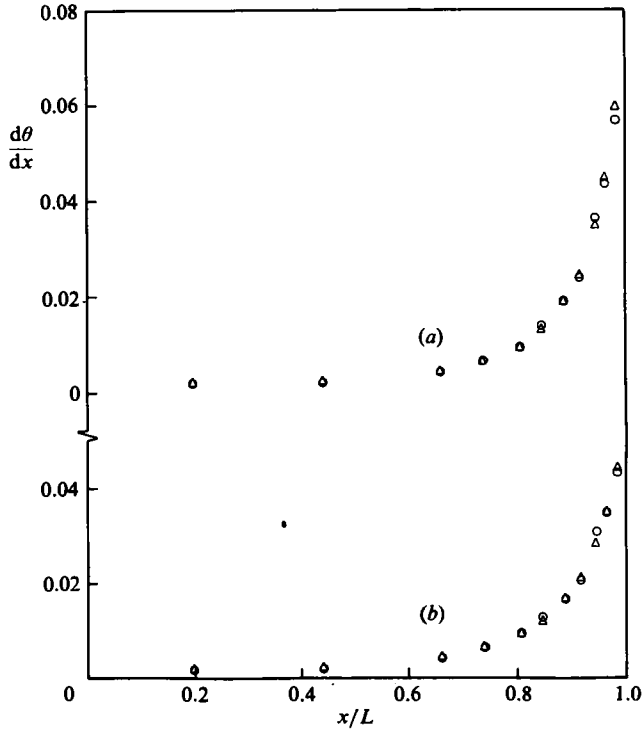
FIGURE 15. Momentum balance (a) with the sting, (b) with the jet:
○, experiment; △, momentum integral equation.
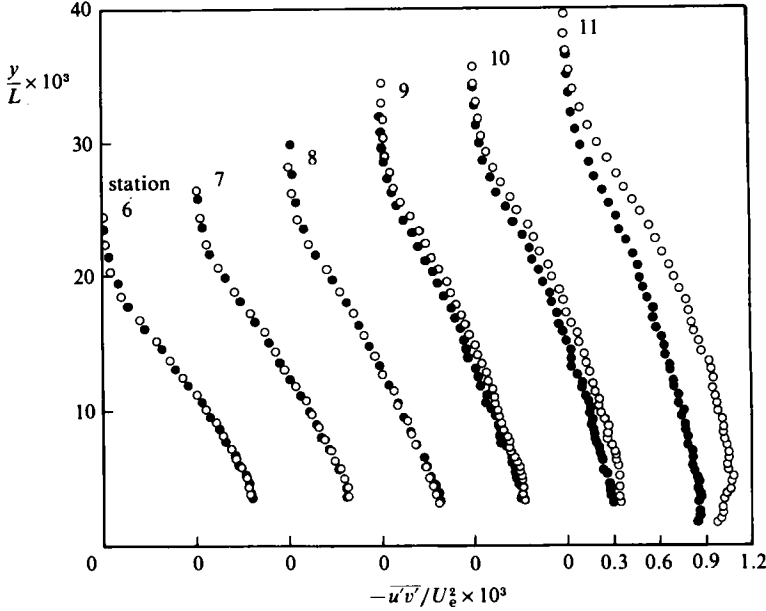
FIGURE 16. Reynolds-shear-stress profiles: $\bigcirc$, with the sting; $\bullet$, with the jet.

values of H at the rear of the model are well below the values usually associated with separation and, as was confirmed by surface-oil-flow visualization, the flow at the rear of the model was always attached.

Finally in this section on integral properties, figure 15 shows the momentum balance in the boundary layer by comparing the measured value of the rate of change of the momentum thickness $\mathrm{d}\theta/\mathrm{d}x$ with that calculated from the momentum integral equation, i.e.

$$\frac{\mathrm{d}\theta}{\mathrm{d}x} = \frac{C_f}{2} - (H+2)\frac{\theta}{U_e}\frac{\mathrm{d}U_e}{\mathrm{d}x} - \frac{\theta}{r_0}\frac{\mathrm{d}r_0}{\mathrm{d}x} + \frac{1}{r_0 U_e^2}\left[\frac{\mathrm{d}}{\mathrm{d}x}\int_0^\infty r(\overline{u'^2}-\overline{v'^2})\,\mathrm{d}y + \frac{\mathrm{d}r_0}{\mathrm{d}x}\int_0^\infty \overline{v'^2}\,\mathrm{d}y\right],$$

where the first three terms were evaluated from the mean-flow measurements and the last term from the turbulence measurements discussed below. The contribution from the Reynolds stresses was very small compared to the contribution from the mean flow.

As will be seen from figure 15, the agreement between the two sides of the momentum integral equation is very good up to station 8 ($x/L = 0.917$) but thereafter there are small differences where the boundary layer thickens rapidly although these differences are not systematic and do not appear to indicate any significant departure from axisymmetric flow.

4.4. Turbulence measurements

Results of the turbulence measurements made at stations 6–11 with and without the jet are presented in figures 16–18. In these figures the relevant turbulence quantity is non-dimensionalized by the square of the velocity U_e at the edge of the layer and the non-dimensional quantity $-\overline{u'v'}/U_e^2$ will be referred to as the shear stress and $\overline{u'^2}/U_e^2$ and $\overline{v'^2}/U_e^2$ as the normal stresses. In general the form of these stresses are similar to those measured by Patel et al. (1974) and Patel, Lee & Güven (1979) in
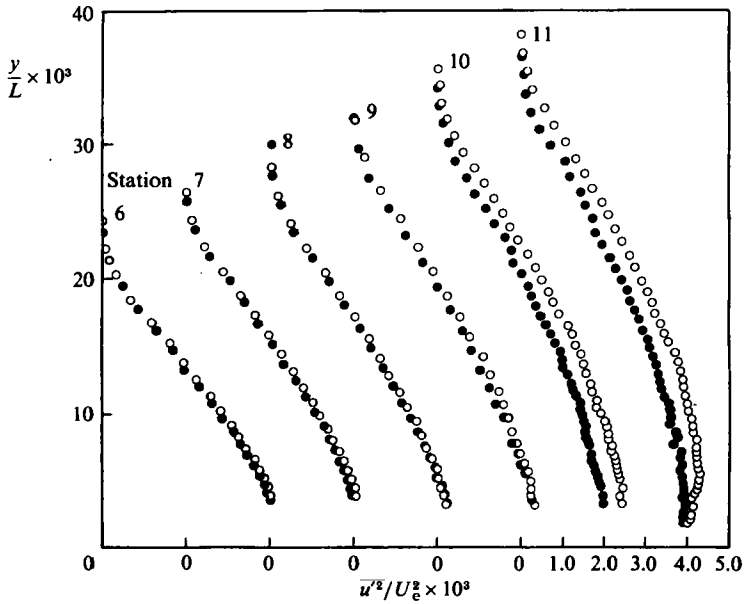
FIGURE 17. Reynolds-normal-stress profiles u'/U_e: $\bigcirc$, with the sting; $\bullet$, with the jet.
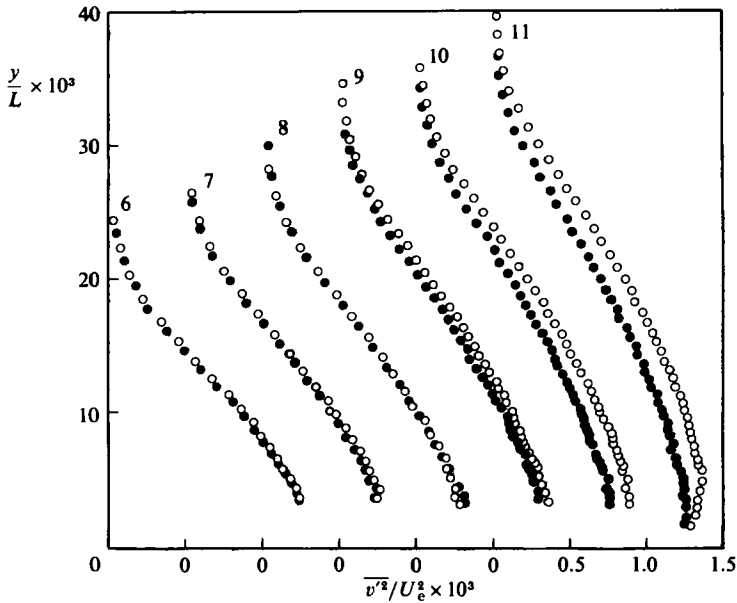
FIGURE 18. Reynolds-normal-stress profiles v'/U_e: $\bigcirc$, with the sting; $\bullet$, with the jet.

thick boundary layers near the tails of bodies of revolution. In particular the present results support the observations made by Patel *et al.* that the level of turbulence in the thick axisymmetric boundary layers appears to be low compared with that in thin two-dimensional layers. It will also be seen that the levels of the various stresses increase significantly when the jet is replaced by the sting.

Derived quantities based on the turbulence measurements are presented in
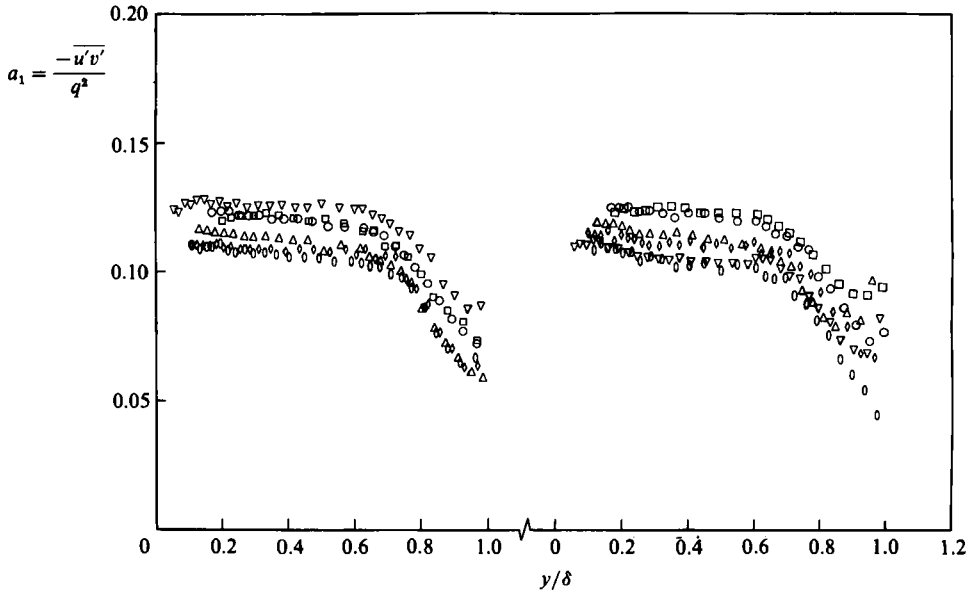
FIGURE 19. Variation of the structure parameter a_1 through the boundary layer with the sting (left), with the jet (right): $\square$, $x/L = 0.848$; $\bigcirc$, 0.888; $\triangle$, 0.917; 0, 0.946; $\diamondsuit$, 0.965; $\triangledown$, 0.985.
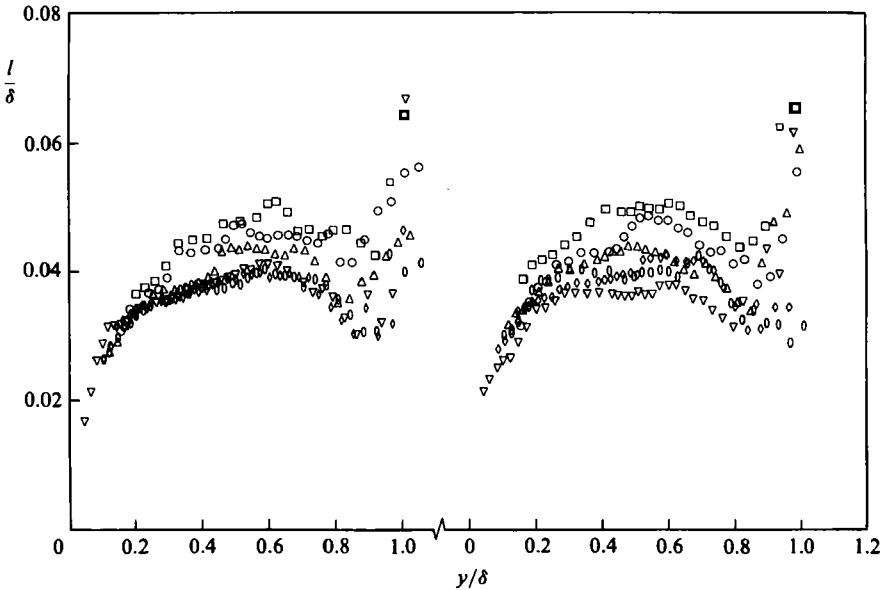
FIGURE 20. Mixing-length profiles. Key as figure 19.

figures 19–21. Figure 19 shows the variation of the ratio of the shear stress to twice the turbulence kinetic energy ($q^2 \equiv \overline{u'^2} + \overline{v'^2} + \overline{w'^2}$ with $\overline{w'^2}$ taken as $\frac{1}{2}(\overline{u'^2} + \overline{v'^2})$). As will be seen, this ratio is significantly below the value 0.15 generally associated with thin two-dimensional layers.

Figures 20 and 21 show the calculated values of the mixing length l ($-\rho\overline{v'u'} = \rho l^2 (\partial u/\partial y)^2$) and the eddy viscosity ϵ ($-\rho\overline{v'u'} = \rho\epsilon\,\partial u/\partial y$). Again the values
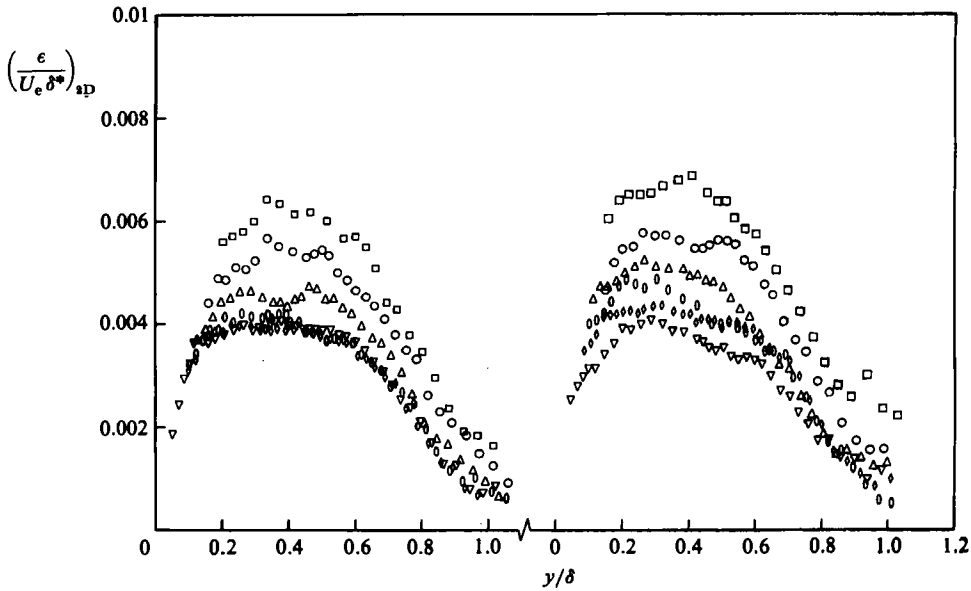
FIGURE 21. Eddy-viscosity profiles. Key as figure 19.

of l and ϵ both appear smaller than the corresponding values in plane two-dimensional flows: for example it is generally accepted that in two-dimensional layers the mixing length levels out at a value of about 0.08δ for $y/\delta > 0.2$ and that the maximum value of the non-dimensional eddy viscosity $(\epsilon/U_e\delta^*)$ is about 0.017. However, it should be pointed out that there is a large variation in the derived values of these parameters for two-dimensional flows for converging and diverging flows on plane surfaces. For example a series of papers by Head and Galbraith (Head 1976; Galbraith & Head 1975; Head & Galbraith 1975; Galbraith 1976) it has been shown that in two-dimensional layers the maximum value of the non-dimensional eddy viscosity is greater than 0.017 in equilibrium layers with adverse gradients, but that in non-equilibrium layers the maximum eddy viscosity tends to lag behind the appropriate equilibrium value. Thus, for example, in a flow with an increasing adverse pressure gradient, that is H increasing, the non-dimensional eddy viscosity is less than it would be in an equilibrium layer with the local values of H and R_θ, while in a relaxing layer there is a significant increase in the non-dimensional eddy viscosity. Both Head (1976) and Sjolander (1980) have shown that convergence or divergence of the flow also has a marked effect on the eddy viscosity, divergence tending to increase the non-dimensional eddy viscosity and convergence to reduce it. Head (1976) points out that this behaviour exactly parallels that of entrainment as discussed by Head & Patel (1970), who explain the effects on entrainment in terms of the spacing of the large eddies that are responsible for the intermittency of the turbulence in the outer region of the layer.

The present layer is subject to an increasing adverse pressure gradient and to convergence, and both these effects on a plane surface would tend to decrease the level of the eddy viscosity. In fact the levels on the non-equilibrium effects as computed by Galbraith for two-dimensional flows (Galbraith 1976) and as measured and computed by Sjolander (1980) show a large amount of scatter, so it is difficult to produce accurate estimates for the present flows, but some estimates have been attempted for the flow at station 6 where the boundary layer is relatively thin. If
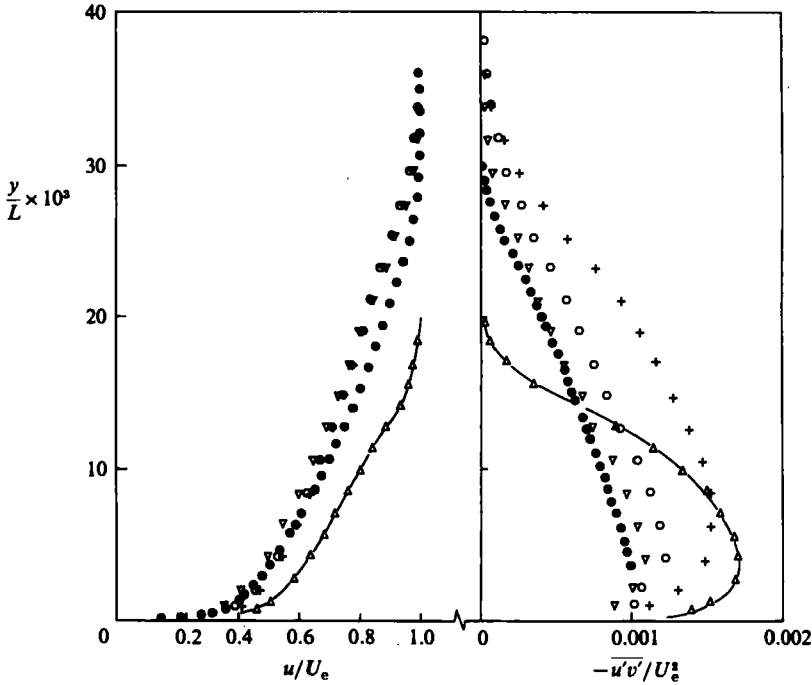
FIGURE 22. Contributions of extra rates of strain in axisymmetric-flow calculations owing to (a) transverse and (b) longitudinal curvature: ∇, (a) and (b); +, (b) only; $\bigcirc$, (a) only; $\bullet$, two-dimensional flow with (b) only; $-\triangle-$, experiment. All results for the flow with the sting at $x/L = 0.946$.

we ignore first the axisymmetric effects and treat the present layer as two-dimensional with the measured pressure distribution then an equilibrium layer with the measured $\bar{H}$ and $\bar{R}_\theta$ would result in a maximum value of $\epsilon/U_e \delta^*$ of about 0.02. The two-dimensional non-equilibrium effects, as measured by $\bar{\theta}$ & $\mathrm{d}\bar{H}/\mathrm{d}x$, would, according to the computed results of Galbraith, give a reduction of between 10 and 30%, i.e. $0.014 < \epsilon/U_e \delta^* < 0.018$. On the other hand if we follow Sjolander and measure the non-equilibrium effects owing to both pressure gradient and convergence by the parameter

$$\left(\frac{1}{U_e}\frac{\mathrm{d}(U_e\theta)}{\mathrm{d}x}\right)_{\mathrm{expt}}\bigg/\left(\frac{1}{U_e}\frac{\mathrm{d}(U_e\theta)}{\mathrm{d}x}\right)_{\mathrm{equil.}},$$

where $[(1/U_e)$ & $\mathrm{d}U_e\,\theta/\mathrm{d}x]_{\mathrm{equil.}}$ is determined from an equilibrium layer with the local values of $\bar{H}$ and R_θ then the reduction in the equilibrium value of $\epsilon/U_e \delta^*$ would be about 50%, i.e. $\epsilon/U_e \delta^* \sim 0.01$. This is close to the measured value and suggests that the reduced levels of shear stress measured in the present investigation, and in that of Patel *et al.*, are at least partially owing to the effects of increasing adverse pressure gradient and flow convergence.

To investigate these effects further use was made of the Bradshaw & Unsworth (1974) program, in which the turbulence kinetic energy is computed and then the Reynolds stress is estimated by assuming it is a given fraction of the kinetic energy. This program contains options for including the effects of additional rates of strain owing to longitudinal curvature and to convergence or divergence associated with transverse curvature, and in all the results presented earlier these effects have been

included. Calculated results obtained by suppressing some of the additional rates of strain are shown in figure 22, where velocity and shear-stress profiles measured and calculated at $x/L = 0.946$ are presented. The shear stress calculated by the full program is in good agreement with the measured stress, although agreement between the calculated and measured velocity profiles is less good. Suppressing the effects of the additional rate of strain due to longitudinal curvature increases the predicted shear stress slightly but produces a negligible change in the mean-velocity profile. However, the effect of suppressing the extra rates of strain owing to convergence because of transverse curvature produces a large increase in the shear stress. The figure also includes the calculated shear stress and mean-velocity profiles at $x/L = 0.946$ in two-dimensional flow with the same pressure gradient, longitudinal curvature and Reynolds number as in the present test on the nacelle. As will be seen the boundary layer is much thinner than that on the nacelle and the maximum shear stress is slightly greater than that calculated on the nacelle when the additional rates of strain owing to convergence are excluded. Together these results demonstrate the importance of the additional rates of strain associated with convergence owing to transverse curvature and show that their effects are included adequately in the program of Bradshaw & Unsworth.

Finally it should be noted that at the rear of the model the full version of the Bradshaw & Unsworth program also predicts an increase in shear stress when the jet is replaced by the sting, although the predicted increase is only about 60 % of the measured increase. This suggests that the increase in turbulence level at the rear of the model when the jet is replaced by the sting is partly owing to the increase in adverse pressure gradient. However, as pointed out in §4.2 the mean-flow streamlines in this region may change from convex to concave when the jet is replaced by the sting and this too would tend to increase the turbulence.

5. Conclusions

The results of the present investigation show that the main effects of replacing a jet by a solid cylindrical sting are as follows: (a) the pressure recovery over the afterbody increases and so the drag decreases: (b) the boundary layer on the afterbody becomes less full, leading to an increase in the displacement thickness and a higher value of the shape parameter H; and (c) the turbulence intensity increases. However, all these effects begin to be significant only very close to the base and the flows with the jet and with the sting are virtually identical for distance from the base greater than about 1 jet diameter in the present case with a jet velocity of 2.5 times the free-stream velocity. It seems likely that similar effects will apply for other jet velocities.

The changes in boundary-layer development are consistent with the stronger adverse pressure gradient for the flow with the sting and it has been shown that the magnitudes of the changes in the mean-flow boundary-layer properties are predicted with reasonable accuracy by an existing boundary-layer program using the measured pressure distributions. This program also predicts a higher Reynolds shear stress, although the predicted difference is only just over half the measured increase. This relative success of prediction methods in which the only information about the external flow is the measured pressure distribution suggests that the changes in boundary-layer development are a direct consequence of the difference between the external flows and are not more directly influenced by the method of simulating the

jet. It should, however, be noted that the existing boundary-layer calculation methods are not satisfactory for predicting fine details of the flow since they are strictly applicable only to thin boundary layers.

Appendix. Integral thicknesses and the momentum equation

In two-dimensional, incompressible flow the displacement and momentum thicknesses given by

$$\bar{\delta}^* = \int_0^\infty \left(1 - \frac{u}{U_e}\right) \mathrm{d}y \quad \text{and} \quad \bar{\theta} = \int_0^\infty \left(1 - \frac{u}{U_e}\right) \frac{u}{U_e} \mathrm{d}y \tag{A 1}$$

occur naturally in the momentum integral equation

$$\frac{\mathrm{d}}{\mathrm{d}x}(U_e^2 \bar{\theta}) + \bar{\delta}^* U_e \frac{\mathrm{d}U_e}{\mathrm{d}x} = \frac{C_f}{2} U_e^2 \tag{A 2}$$

or

$$\frac{\mathrm{d}\bar{\theta}}{\mathrm{d}x} = \frac{C_f}{2} - \frac{\bar{\theta}}{U_e} \frac{\mathrm{d}U_e}{\mathrm{d}x} (2 + \bar{H}), \tag{A 3}$$

where $\bar{H} = \bar{\delta}^*/\bar{\theta}$. Also in two-dimensional flow these thicknesses have a clear physical meaning so that, for example, $\bar{\delta}^*$ is the displacement of the surface required to correct for the mass-flow defect in the boundary layer, that is

$$\int_{\bar{\delta}^*}^\infty \rho U_e \, \mathrm{d}y = \int_0^\infty \rho u \, \mathrm{d}y. \tag{A 4}$$

Furthermore the 'shape' factor $\bar{H}$ as its name implies is a useful guide to the shape and hence the state of the boundary-layer profile. In axisymmetric flows with thick boundary layers, however, the situation is more complicated. The momentum integral equation can still be written in a form similar to (A 2), i.e.

$$\frac{\mathrm{d}}{\mathrm{d}x}(r_0 U_e^2 \theta) + r_0 \delta^* U_e \frac{\mathrm{d}U_e}{\mathrm{d}x} = r_0 \frac{C_f}{2} U_e^2, \tag{A 5}$$

where

$$\delta^* = \int_0^\infty \left(1 + \frac{y}{r_0} \cos\phi\right)\left(1 - \frac{u}{U_e}\right) \mathrm{d}y,$$

$$\theta = \int_0^\infty \left(1 + \frac{y}{r_0} \cos\phi\right)\left(1 - \frac{u}{U_e}\right) \frac{u}{U_e} \mathrm{d}y. \tag{A 6}$$

In this case, however, δ^* and θ do not correspond to thicknesses of physical significance. For example the physical displacement thickness δ_p^* defined in an analogous manner to (A 4) gives

$$\int_{\delta_p^*}^\infty \rho \left(1 + \frac{y}{r_0} \cos\phi\right) U_e \, \mathrm{d}y = \int_0^\infty \rho \left(1 + \frac{y}{r_0} \cos\phi\right) u \, \mathrm{d}y \tag{A 7}$$

or
$$\int_0^{\delta_p^*} \left(1 + \frac{y}{r_0}\cos\phi\right) U_e \, dy = \int_0^\infty \left(1 + \frac{y}{r_0}\cos\phi\right)(U_e - u) \, dy \qquad (A\,8)$$

or
$$\delta_p^* + \frac{1}{2}\frac{\delta_p^{*2}}{r_0}\cos\phi = \delta^*.$$

Similarly $\theta_p + \frac{1}{2}(\theta_p^2/r_0)\cos\phi = \theta$, where θ_p is the physical momentum thickness.

In the present investigation where the boundary layers are only of moderate thickness $\delta_p^* = \delta^*$ and $\theta_p = \theta$, so that we can refer to δ^* and θ as the displacement thickness and momentum thickness respectively. However, as shown in figures 12–14 there are significant differences between these thicknesses and the values obtained using the two-dimensional, or planar, definitions $\bar{\delta}^*$ and $\bar{\theta}$ (A 1).

REFERENCES

ABEYOUNIS, W. K. & PUTNAM, L. E. 1980 Investigation of the flow field surrounding circular-arc boat-tail nozzles at subsonic speeds. *NASA TP*-1633.

BRADSHAW, P. 1966 The turbulent structure of equilibrium layers. *NPL Aero. Rep.* 1184.

BRADSHAW, P. 1971 *Introduction to Turbulence and its Measurements*. Pergamon.

BRADSHAW, P. & UNSWORTH, K. 1974 An improved Fortran program for the Bradshaw–Ferris–Atwell method of calculating turbulent shear layers. *Imperial College Aero. Rep.* 74–02.

CEBECI, T. 1970 Laminar and turbulent incompressible boundary layers on slender bodies of revolution in axial flow. *Trans. ASME* D: *J. Basic Engng* 92, 545–550.

CHASE, D. M. 1972 Mean velocity profile of a thick turbulent boundary layer along a circular cylinder. *AIAA J.* 10, 849–850.

DURST, F., LAUNDER, B. E., SCHMIDT, F. W. & WHITELAW, J. H. (eds) 1979 *Turbulent Shear Flows I*. Springer.

GALBRAITH, R. A. McD. 1976 Contributions to the analysis and prediction of turbulent boundary layers. Ph.D. Dissertation, University of Cambridge.

GALBRAITH, R. A. McD. & HEAD, M. R. 1975 Eddy viscosity and mixing length from measured boundary layer developments. *Aero Quart.* 26, 133–154.

GREEN, J. E., WEEKS, D. J. & BROOMAN, J. W. F. 1973 Prediction of turbulent boundary layers and wakes in compressible flow by a lag-entrainment method. *Aero. Res. Counc. R & M* 3791.

HEAD, M. R. 1976 Eddy viscosity in turbulent boundary layers. *Aero Quart.* 27, 270–275.

HEAD, M. R. & GALBRAITH, R. A. McD. 1975 Eddy viscosity and entrainment in equilibrium boundary layers. *Aero Quart.* 26, 229–242.

HEAD, M. R. & PATEL, V. C. 1970 Improved entrainment method for calculating turbulent boundary layer development. *Aero. Res. Counc. R & M* 3643.

HESS, J. L. & MARTIN, R. P. 1974 Improved solution for potential flow about arbitrary axisymmetric bodies by the use of a higher-order surface source method. Part I. Theory and results. *NASA CR*-134694.

LAI, E. 1983 Boundary layer development on nacelle afterbodies. Ph.D. Dissertation, University of Cambridge.

LUDWIEG, H. & TILLMANN, W. 1949 Untersuchungen über die Wandschubspannung in turbulenten Reibungsschichten. English translation, Investigation of the wall-shearing stress in turbulent layers, is available as *NACA TM*-1285.

PATEL, V. C. & LEE, Y. T. 1977 Thick axisymmetric turbulent boundary layer and near wake of a low-drag body of revolution. *IIHR Rep. No.* 210, University of Iowa.

PATEL, V. C., LEE, Y. T. & GÜVEN, O. 1979 Measurements in the thick axisymmetric turbulent boundary layer and the near wake of a low-drag body of revolution. In *Turbulent Shear Flows I* (ed. F. Durst, B. E. Launder, F. W. Schmidt & J. H. Whitelaw), pp. 137–153. Springer.

PATEL, V. C., NAKAYAMA, A. & DAMIAN, R. 1974 Measurements in the thick axisymmetric turbulent boundary layer near the tail of a body of revolution. *J. Fluid Mech.* 63, 345–367.

PUTNAM, L. E., ABEYOUNIS, W. K. 1976 Experimental and theoretical study of flow fields surrounding boat-tail nozzles at subsonic speeds. *AIAA Paper No.* 76–675.

REUBUSH, D. E. 1974 Experimental study of the effectiveness of cylindrical plume simulators for predicting jet-on boat-tail drag at Mach numbers up to 1.30. *NASA TN* D-7795.

SJOLANDER, S. A. 1980 Eddy viscosity in two-dimensional and laterally strained boundary layers. Ph.D. Dissertation, University of Cambridge.

SPALDING, D. B. 1961 A single formula for the law of the wall. *Trans. ASME* E: *J. Appl. Mech.* **28**, 455–458.

THOMPSON, B. G. J. 1965 A new two-parameter family of mean velocity profiles for incompressible turbulent boundary layers on smooth walls. *Aero Res. Counc. R & M* 3463.

WILMOTH, R. G. 1980 Viscous–inviscid calculations of jet entrainment effects on the subsonic flow over nozzle afterbodies. *NASA-TP*-1626.